

Research Article

Experiment Investigation and Numerical Simulation of Snowdrift on a Typical Large-Span Retractable Roof

Zhenggao Cao ^{1,2}, Mengmeng Liu,^{1,2} and Pengcheng Wu^{1,2}

¹Key Lab of Structures Dynamic Behavior and Control of the Ministry of Education, Harbin Institute of Technology, Harbin 150090, China

²Key Lab of Smart Prevention and Mitigation of Civil Engineering Disasters of the Ministry of Industry and Information Technology, Harbin Institute of Technology, Harbin 150090, China

Correspondence should be addressed to Zhenggao Cao; caozg75@163.com

Received 5 September 2019; Revised 26 November 2019; Accepted 2 December 2019; Published 26 December 2019

Academic Editor: Toshikazu Kuniya

Copyright © 2019 Zhenggao Cao et al. This is an open access article distributed under the Creative Commons Attribution License, which permits unrestricted use, distribution, and reproduction in any medium, provided the original work is properly cited.

Retractable roofs are commonly used in designing large-span stadiums because of their versatility. However, retractable roofs are subject to sudden changes in shape, and thus, factors in addition to those considered for conventional roofs need to be taken into account. In particular, retractable roofs are considerably more sensitive to snow loads because their shapes are complex, and snowdrift on roofs may lead to difficulties for the operating of retractable roofs. To investigate the distribution of snow on retractable roofs, this study proposes a method based on a numerical simulation of snowdrift obtained using the Euler–Euler method in multiphase flow theory. This numerical model employs a mixture model by using the commercial computational fluid dynamics (CFD) software FLUENT. A suitable turbulence model is selected for the simulation through verification against two-dimensional (2D) data obtained from field measurements reported in previous studies. However, the snow load on retractable roofs cannot be determined by a 2D distribution easily. The accuracy of predicting the overall distribution of snow load on roofs was verified by experiments conducted on a horizontally retractable roof. The results show that a nonuniform snow distribution on such roofs is distinct and should be considered.

1. Introduction

Frequent snow and ice storms occur all over the world, and the partial structural overload and collapse of the roofs of buildings owing to the unbalanced distribution of snow on them are common. Research on the snow load on roofs is thus important for the safety of structures, particularly long-span spatial structures.

Three methods are commonly used to investigate wind-induced snowdrift: field measurements, wind tunnel experiments, and numerical simulations. These methods supplement one another and each offers its own advantages and disadvantages. Field observations are essential in studies on wind-induced snowdrift and are known to provide the bulk of relevant data. However, the results obtained are often affected by various external factors and

the accumulation of data from field observations is a time-consuming process. Wind tunnel experiments are based on the motion mechanism of snow particles, reasonable similarity relations, and appropriate granular materials simulating snow particles to carry out rapid predictions of snowdrift [1]. However, it is difficult at present to satisfy all similarity criteria and several of them may be ignored depending on the situation. Numerical simulations are popular and have been widely adopted in recent years because they are cost effective, highly efficient, and easily controllable [2]. Moreover, no similarity problems occur when studying large-scale buildings using simulations. However, many methods based on numerical simulations are available, and in the absence of a uniform standard, selecting a suitable method is challenging. This is therefore one of the goals of this study.

Two methods based on numerical simulations are mainly used to implement two-phase flow theory: the Euler–Lagrange method and the Euler–Euler method.

The Euler–Lagrange method assumes that the snow phase is discrete in the air. Newton’s law of motion is used to obtain the trajectory of a single snow particle and the volume of snow is then distributed by integration. Alhajraf [3] applied the Euler–Lagrange method to establish a FLOW-3D model to investigate snowdrift around a snow fence and found that the results were in agreement with those of measurements. Okaze et al. [4] proposed a simulation method based on the coupling of large eddy model (LES) and Lagrangian method and applied this method to simulate the development of snow particle migration process under low wind speed. This study found that at the initial stage, the snow particle transport mainly relies on the airflow to keep the saltation of particles; with the development of time, the particle splash and rebound caused by the collision occupy the dominant position of the particle transport. Zhou et al. [5] applied the CFD-DEM method to simulate the snowdrift on a typical stepped roof in 2D both considering the cohesion and collision between snow particles, and the snow distribution was verified to be similar to that in field measurement and wind tunnel test.

The Euler–Euler method assumes that both the air and the snow phases are continuous, and it is solved by adding the governing equation of the snow phase to the control equation of the air phase and most current numerical simulations of wind-induced snowdrift use the Euler–Euler method.

Uematsu et al. [6] conducted a numerical simulation of the distribution of snowdrift around a snow fence. They considered the saltation and suspension processes in the simulation and proposed a three-dimensional (3D) simulation to yield results close to those of field observations. However, the method only considers the rate of snow mass transfer and ignores the influence of wind turbulence. In previous studies, researchers were more concerned with snowdrift on the ground. Beyers et al. [7] used FLOW-3D to simulate snowdrift around a cube with a length of 2 m. They used the standard k - ϵ model and an improved turbulent wall function to consider the effect of the drift of the snow particles on the effective length of roughness of the snow surface and compared the results with those of measurement at the SANAE IV scientific research station in Antarctica. They concluded that the results of snowdrift were in good agreement with the measured values in terms of both shape and magnitude. Beyers and Waechter [8] used Fluent to simulate snowdrift around two side-by-side cubic buildings, three side-by-side overhead buildings, and dormitory complex of the Antarctic scientific research base. Embedded user-defined functions and mesh deformation were used to model changes in snowdrift over time owing to snow deposition or erosion. Although the results of the numerical simulation were in good agreement with measurements, because the authors had used the k - ϵ turbulence model in the simulation, where this model has inherent deficiencies, they also opined that better results can be obtained when using improved two-equation models. Tominaga et al. [9] pointed

out that the governing equations used in previous studies could not describe the changes of flow field around the building accurately. The boundary conditions such as threshold velocity and snow phase concentration have great influence on the simulation results, and a new method is proposed based on the Renault Time-Rate Method (RANS) and the reliability of the new method is verified by comparing the simulation result of snow distribution around the cube with the measured results.

Recent years, researchers have witnessed more research on the snow load on roofs. Thiis et al. [10] conducted field measurements and numerical simulations on the curved roof of a sports hall located in Oslo. Sun et al. [11] simulated the snowdrift on a long-span membrane roof and mechanical performance of the membrane structure under nonuniform snow load was also studied. However, most studies have focused on specific buildings and research on the general rules of patterns of snow distribution on large-span roofs has rarely been reported. Considering the diversity of the shapes of large-span roofs, many scholars have suggested that for such structures with complex roof shapes, both numerical simulations and wind tunnel tests should be carried out to determine the coefficient of snow distribution.

As the name implies, the retractable roof is a type of roof structure that allows the building to be used with an “open” or “closed” roof. As a type of large-span structure with a strong comprehensive function, the retractable roof saves energy and is environmentally friendly, in line with current developments in architectural technologies. Retractable roofs are widely used; however, owing to their discontinuous shape, more complex snow distribution occurs on them. Moreover, unlike the typical large-span roof, snowdrift on retractable roofs may cause serious operational issues.

Research relating to snow loads on retractable roofs is scant, no specific provisions for this type of structure are available and only certain introductory articles are available for reference.

This study focuses on snow loads on a typical horizontally retractable roof, which was widely used in long-span roof structures as shown in Figure 1, and only the “closed” state of the retractable roof is considered because buildings should be generally covered when it is snowing. To validate the accuracy of the numerical simulation of snow load distribution, experiments on a horizontally retractable roof model were carried out to determine the accuracy of predicting the overall snow load distribution and the regularity of snowdrift on such a roof. Finally, distributions of snow on two other typical retractable roofs were investigated using the CFD method.

2. Numerical Method and Validation

2.1. Governing Equations. Euler–Euler description in multiphase flow theory is used for the simulation in this study, in which both snow and air are treated as continuous phases. There are three Euler–Euler-based multiphase models in FLUENT: the VOF, mixture, and Eulerian models. Among them, the mixture model exhibits superior stability and low computation requirements while delivering nearly the same

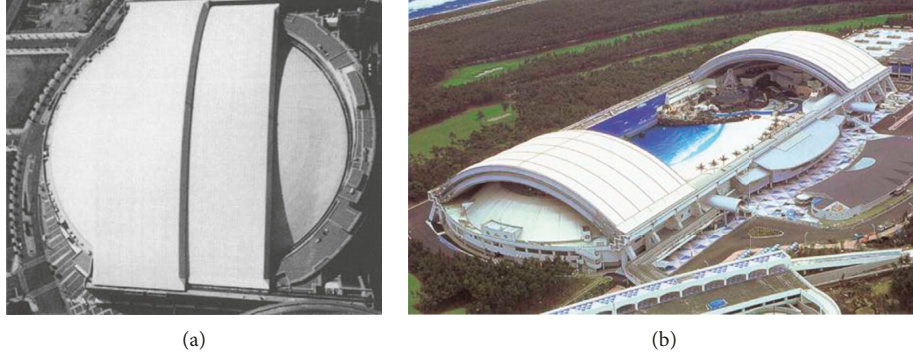


FIGURE 1: Typical horizontally retractable roof. (a) Sky Dome, Canada. (b) Ocean Dome, Japan.

precision as the Euler model [12]; thus, the mixture model is used in this study.

In the mixture model, mixture phases, including air and snow, share the same equations of mass continuity and conservation of momentum, as per equations (1) and (2). It is assumed that only one-way coupling exists between the air and the snow phases, and equations of the momentum and turbulence of air can be regarded as unaffected by the airborne snow.

Moreover, the continuity equation for the snow phase is provided by equation (3) [13]:

$$\frac{\partial}{\partial t} (\rho_m) + \nabla \cdot (\rho_m \vec{v}_m) = 0, \quad (1)$$

$$\frac{\partial(\rho_m \vec{v}_m)}{\partial t} + \nabla \cdot (\rho_m v_m \vec{v}_m) = -\nabla \cdot p + \nabla \cdot \left[\mu_m (\nabla \vec{v}_m + \nabla \vec{v}_m^T) \right] + \rho_m \vec{g} + \vec{F}, \quad (2)$$

$$\frac{\partial(\rho_s f_2)}{\partial t} + \nabla \cdot (\rho_s f_2 \vec{v}_m) = 0, \quad (3)$$

where $\rho_m = \sum_{k=1}^2 f_k \rho_k$ is the density of the air and snow mixture; $\vec{v}_m = \sum_{k=1}^2 f_k \rho_k \vec{v}_k / \rho_m$ is the average velocity of the mixture phase; f_k is the volume fraction of the air phase ($k=1$) and snow phase ($k=2$); p is the pressure of the air field; and $\mu_m = \sum_{k=1}^2 \alpha_k \mu_k$ represents hybrid viscosity.

The governing equations selected for the simulation do not consider the effect of slip velocity and mass exchange between the phases in their source terms. There is no credible evidence for the determination of the slip velocity between the phases, and Hao et al. [14] found no significant difference in the results without considering the relative slip velocity. Moreover, it is difficult to guarantee its convergence when considering mass exchange between phases, and thus its effect was ignored in the simulation.

2.2. Deposition and Erosion Model. Wall shear stress, which is used to determine the state of movement of snow particles, is an important parameter in snowdrift. Snow particles begin moving when the wall shear stress τ on the

snow surface exceeds the threshold wall shear stress τ ; otherwise, the snow particles remain stationary. In the numerical simulation, the wall shear stress τ is replaced by frictional velocity u_* and defined as the following relation:

$$u_* = \sqrt{\frac{\tau}{\rho}} = \frac{\kappa u(z)}{\ln(z/z_s)}, \quad (4)$$

where κ refers to the Von Karman constant that is equal to 0.4 and z_s is the height of aerodynamic roughness over the snow surface, which was set to 3.0×10^{-5} m. The snow mass flux of erosion q_{ero} is simplified as a function of the frictional velocity and bonding strength of the snowdrift. The deposition flux q_{dep} is calculated as a function of the snow fraction f and snowfall velocity w_f ([15]):

$$\begin{aligned} q_{\text{ero}} &= A_{\text{ero}} (u_{*t}^2 - u_*^2), \\ q_{\text{dep}} &= \rho_s f w_f \frac{u_{*t}^2 - u_*^2}{u_{*t}^2}, \end{aligned} \quad (5)$$

where A_{ero} is a proportionality coefficient, set to 7.0×10^{-4} ; u_{*t} is the threshold frictional velocity, set to 0.2 m/s [9]; and w_f is snowfall velocity, assumed to be 0.2 m/s.

The thickness of snow distribution changes with erosion or deposition. In this case, q_s is uniformly used to replace q_{dep} or q_{ero} and the change in the thickness of snow distribution over time is calculated as follows:

$$dh = -\frac{q_s}{\rho_s \gamma} dt, \quad (6)$$

where γ is the maximum volume fraction of the snow phase.

The steady method simplifies the snowdrift process and is only valid for relatively small snowdrifts; however, the results of prediction of the steady method have been shown to reasonably reproduce field observations or wind tunnel test data [9]. In the steady simulation, the erosion/deposition of snow is regarded as in a steady state and the rate of change of snow depth per unit time q_s/ρ_s remains constant. Thus, the time integration in equation (6) becomes

$$h(t) = h_0 + \frac{q_s}{\rho_s} \Delta t, \quad (7)$$

where h_0 is the initial depth of snow.

2.3. Inflow Boundary Conditions. The fully developed inlet wind velocity profile is determined from the power law profile:

$$v(z) = v_0 \left(\frac{z}{z_0} \right)^\alpha, \quad (8)$$

where v_0 and z_0 are the reference velocity and reference height, respectively.

Furthermore, the turbulent kinetic energy k and turbulent kinetic dissipation rate ε were also provided for the turbulence characteristic:

$$\begin{aligned} k &= \frac{3}{2} (vI)^2, \\ \varepsilon &= C_\mu^{3/4} \frac{k^{3/2}}{l}, \end{aligned} \quad (9)$$

where C is the empirical coefficient that is selected as 0.09 and l and I are the turbulence length scale and turbulence intensity, respectively, which are determined by the following equations[16]:

$$l = \begin{cases} 100 \left(\frac{z}{30} \right)^{0.5}, & 30 \text{ m} < z < Z_G, \\ 100, & z \leq 30 \text{ m}, \end{cases} \quad (10)$$

$$I = \begin{cases} 0.1 \left(\frac{z}{Z_G} \right)^{-\alpha' - 0.05}, & z_b < z < Z_G, \\ 0.1 \left(\frac{z_b}{Z_G} \right)^{-\alpha' - 0.05}, & z \leq z_b. \end{cases} \quad (11)$$

On the assumption of unidirectional coupling, the inlet velocities of the snow and air phases were considered to be the same. The spatial distribution of the snow phase is divided into creep, saltation, and suspension, in which the transport volume of the slow-moving layer is relatively small. Thus, only the saltation and suspension of the snowdrift are considered. The snow mass transfer rates in the saltation ($z \leq h_s$) and suspension ($z > h_s$) layers are expressed as equations (12) and (13) according to actual measurements taken by Pomeroy and Gray and Pomeroy and Male [17, 18]:

$$f = \begin{cases} \frac{0.68\rho}{u_p u_* g h_s \rho_s} u_{*t} (u_*^2 - u_{*t}^2), & z \leq h_s, \\ \frac{0.8 \exp \left[-1.55 (4.78 u_*^{-0.544} - z^{-0.544}) \right]}{\rho_s}, & z > h_s, \end{cases} \quad (12)$$

where u_p is the average velocity of the snow particle in the saltation layer and is set as $2.8 u_{*t}$ and h_s is the average height of the saltation layer, which is determined by the following equation [17]:

$$h_s = 1.6 \frac{u_*^2}{2g}. \quad (13)$$

Note that the friction velocity u_* at the inflow boundary should exceed the threshold friction velocity to initiate snowdrift.

2.4. Optimization and Validation of the Turbulence Model. In previous studies, various turbulence models have been employed in snowdrift simulation. Tominaga and Mochida [19] used a modified version of the k - ε model in a snowdrift simulation and compared the results with those of the standard k - ε model. Beyers et al. [7] adopted the standard k - ε model and indicated that it is necessary to perform a critical examination of the influence of inaccuracies in the isotropic turbulence assumption on snow accumulation and erosion. Okaze [20] developed a new k - ε model that incorporates the effects of snow particles on a flow field and verified the accuracy of the new model by comparison with the wind tunnel test. Although many different turbulence models have been employed in the literature, the results obtained by these models are in strong agreement with field observations or test data.

In this study, in order to select a suitable turbulence model, different turbulence models were used to simulate the snow load on a stepped flat roof. The stepped flat roof model adopted was a 1 : 1 model by Tsuchiya et al. [21] used in field observations carried out on the ground of the Hokkaido Institute of Technology (Sapporo, Japan). A sketch of the model is illustrated in Figure 2 and the parameters used in the CFD simulation are listed in Table 1. The snow density is 150 kg/m^3 , the snow particle terminal velocity w_f is 0.2 m/s , and the threshold friction velocity is 0.2 m/s , and considering that the snowing duration is unavailable and to get a relatively stable, fully developed snowdrift result, an assumed snowing duration $\Delta t = 24 \text{ h}$ is adopted in the simulation.

Figure 3 compares the normalized snow depth obtained by different turbulence models along the line of measurement and gives the distribution of ratio of friction velocity above the lower roof to threshold friction velocity. The snowdrift obtained by field observations was divided into four sections according to its features to clarify the assessment. The x -axis represents the relative position on the roof, and H was 0.9 m . The y -axis represents the normalized snow depth at any point, and S and S_d are the measured snow depths at any point and the average snowfall, respectively. Drifting sections I and II show that all three turbulence models underestimated the effect of erosion, and the results of the realizable k - ε and k - kl - w models were closer to the snowdrift reported by field observations in terms of shape. SST k - w was not accurate at estimating the location of extreme points in the erosion zone. Comparing the models in sections III and IV, the results obtained by the realizable k - ε model yielded the closest distribution to field observations and the result was more conservative. The other two methods were inadequately estimated for snow accumulation. From the above

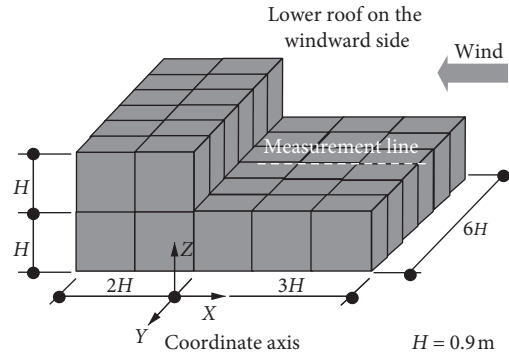


FIGURE 2: Sketch of model [2].

TABLE 1: Computation conditions.

Conditions	Settings
Computational domain	220 m (x) × 40 m (y) × 24 m (z)
Number of elements	Approximately 1,500,000
Minimum mesh size	0.04 m
Inflow boundary	Wind velocity profile (see equation (8)), where v_0 and z_0 are 7.4 m/s and 0.9 m, respectively Snow fraction profile (see equation (12))
Outflow boundary	Zero gradient condition; the wind velocity gradient $\partial u/\partial n$ and snow fraction gradient $\partial f/\partial n$ are set to zero (outflow)
Upper face and side	Zero gradient condition for all variables; the normal components of the wind velocity with respect to the boundaries are set to zero (symmetry)
Building and ground surface	No-slip boundary condition (wall), except that the wall roughness $z_0 = 5.0 \times 10^{-5}$ for the snow surface
Turbulence model	SST $k-w$ model, $k-kl-w$ model, realizable $k-\epsilon$ model
Multiphase model	Mixture model

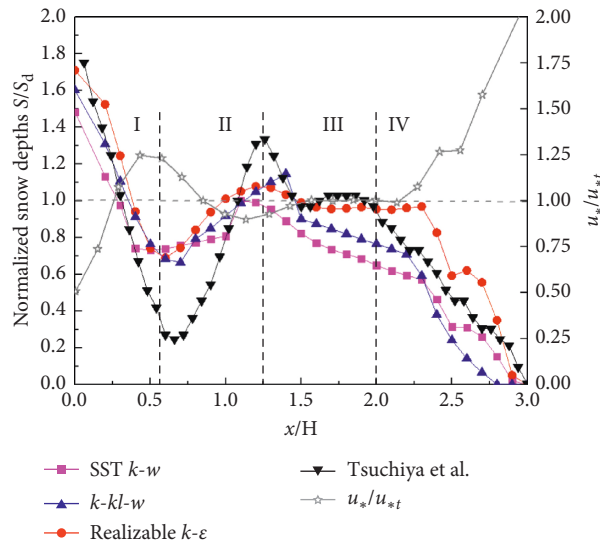


FIGURE 3: Normalized snow depth obtained by different turbulence models along the line of measurement.

analysis, the results obtained by the realizable $k-\varepsilon$ model exhibited stronger agreement with field observations. Thus, the realizable $k-\varepsilon$ model was selected as turbulence model for the subsequent CFD simulation.

3. Experimental Validation of Snowdrift on Horizontally Retractable Roofs

Although CFD simulations have been shown to provide relatively effective reductions of the snow depth along the line of measurement, snow distribution on certain large-span or complex roofs, such as retractable roofs, cannot be described using only a simple 2D distribution. Therefore, to determine whether the CFD simulation method can accurately predict snow distribution on such roofs, both experiments and numerical simulations were conducted on snow distribution using a small-scale, horizontally retractable roof model.

3.1. Experimental System

3.1.1. Experimental Facility. A majority of scholars use wind tunnels to conduct wind-induced snowdrift tests. The simulation of snowdrift in a building wind tunnel is implemented by diverting precovered snow using an incoming wind field. The experimental subjects are generally flat surface models, and thus it is reasonable to apply a uniformly distributed layer of snow ahead of time. However, when the subject is nonplanar, its curved surface makes it difficult to uniformly distribute snow on the large-span roof.

The Harbin Institute of Technology has independently proposed the Snow-Wind Combined Experimental Facility composed of six assembled fans in a “power” section, as shown in Figure 4. It forms a stable wind field through a “diversion” section. A snowfall simulator is set up in the wind field to provide a stable snow environment and simulate the natural snowfall process. Moreover, the structure of the equipment is assembly type, which is convenient for disassembly, removal, and transformation. A stable wind speed range of 0.5 to 11.5 m/s was used in the test section and natural snow particles were used in the experiments [22].

3.1.2. Model Information. No confirmed prototype of the architecture and related conditions was available for the test investigation. According to a typical form of a horizontally retractable roof, the prototype roof span was 30 m × 60 m, the rise-to-span ratio was 1:10, the specific length of the fixed roof on both sides was 21 m, the two retractable roofs in the middle were 9 m × 30 m, and the span ratio was 1:10.

The geometric scale ratio of the test was 1:30. The model was constructed from plywood and timber framing and had sufficient strength and rigidity. As illustrated in Figure 5, the fixed roof was 1/10th of the cylindrical shell surface and the central part formed the retractable roof. Moreover, to obtain an accurate snow distribution, measurement points were set every 5 cm in the horizontal projection area.

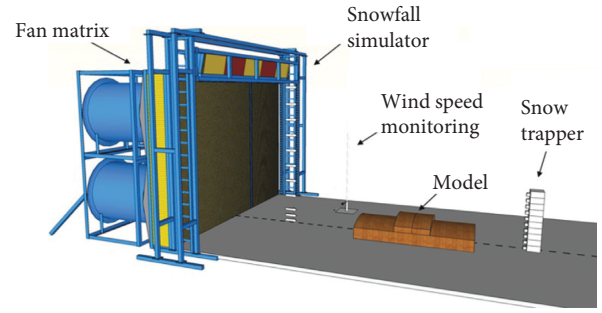


FIGURE 4: Snow-wind combined experimental facility.

3.1.3. Similarity Criterion and Operating Conditions. Reliable experimental modeling at scale depends on an appropriate similarity criterion. Several similarity criteria are available that are, however, incompatible. Thus, the similarity criterion must be selected according to its relevance.

According to the test scheme of the French Jules Verne Climatic Wind Tunnel [3], the equation for the number of similarities was determined based on the Froude number, according to the number of migrating particles in the jump layer. Furthermore, the wind speed and simulation time of the test were established on the basis of parameters similar to those of equations (14)–(19), such as the Reynolds' number limit [23–29]:

$$\left(1 - \frac{U_0}{U}\right) \left(\frac{U^2}{Lg}\right)_p = \left(1 - \frac{U_0}{U}\right) \left(\frac{U^2}{Lg}\right)_m, \quad (14)$$

$$\left(\frac{UT}{L}\right)_p = \left(\frac{UT}{L}\right)_m, \quad (15)$$

$$\left(\frac{u_{*t}^3}{2g\nu}\right)_m \geq 30, \quad (16)$$

$$\left(\frac{u_{*t}^2}{D_p g} \cdot \frac{\rho}{(\rho_p - \rho)}\right)_p = \left(\frac{u_{*t}^2}{D_p g} \cdot \frac{\rho}{(\rho_p - \rho)}\right)_m, \quad (17)$$

$$\left(\frac{\rho_p}{\rho}\right)_m \geq 600, \quad (18)$$

$$\left(\frac{u_{*t}^2}{Lg} \cdot \frac{\rho}{(\rho_p - \rho)}\right)_p = \left(\frac{u_{*t}^2}{Lg} \cdot \frac{\rho}{(\rho_p - \rho)}\right)_m, \quad (19)$$

where L is the reference length of the structure, D_p is particle diameter, T is the time needed for the experiment, ρ_p is the density of the particles, ρ is air density, and U and U_0 are the reference wind speed and threshold reference wind speed, respectively. The air density was set to 1.341 kg/m³ (when the temperature = −10°C), particle density for the model was set to 910 kg/m³, and that for the prototype was set to 300 kg/m³ (the subscript p represents the prototype and m represents model). Furthermore, u_{*t} is the threshold frictional velocity, g is gravitational acceleration, and ν is kinematic viscosity, which varies from 1.32×10^{-5} to 1.67×10^{-5} m² s^{−1} and was set to 1.5×10^{-5} m² s^{−1} in this study.

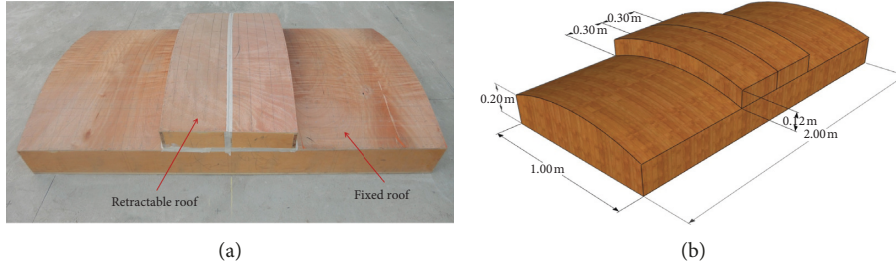


FIGURE 5: Schematic of size and shape of the test model. (a) Photograph of the test model. (b) “Closed” state.

Artificial snow was used in the experiments. To eliminate the differences in particle properties, snow particles used in the experiments were all produced on the same day (01/20/2017) by a single snowmaker. Fresh snow produced by a snowmaker is unsuitable for experiments because of its high moisture content. It also needs to be stored in a sheltered area for at least five days prior to the experiments. The physical properties of the artificial snow particles were measured before the experiments. In particular, the diameter and shape of the particles were observed by an optical microscope and the repose angle as determined by accumulated experiments was 45° . All building models were constructed from wood, and the friction angle between wood and artificial snow was approximately 50° . The shape of the snow particles is illustrated in Figure 6, and a comparison of the physical parameters of the real and artificial snow particles is provided in Table 2.

Taking the Harbin facility as a reference, a type-B landform of the atmospheric boundary layer was adopted. The basic wind pressure in the 50-year recurrence interval was 0.5 kN/m^2 , and the wind speed of the test prototype was determined to be 0.45 times that of the 50-year recurrence interval, according to the historical data [30]. The monitoring point for the reference wind speed point was located 0.2 m above the ground (corresponding to the height of 6 m of the prototypical building roof). According to the similarity criteria, the experimental wind speed was 2.5 m/s (at a height of 0.2 m) and the experimental parameters are shown in Table 3. As indicated in Table 4, all similarity ratios were satisfied after each parameter was reduced by the scale ratio except the value ρ_p/ρ . Kind [25] has noted that this ratio need not be the same in the prototype and the model, but the ratio $\rho_p/(\rho_p - \rho)$ should always be close to one. In this section, the value of this ratio for prototype and model were approximately 1.01 and 1.002, respectively.

3.1.4. Information on Experimental Conditions. To obtain wind speed data near the model during the test, a thermal anemometer with a long probe was used to monitor the experimental wind speed prior to the experiments. The accuracy of measurement of wind speed was 0.01 m/s. The profiles of the normalized mean wind speed (the ratio of the measured wind speed $U(z)$ to the reference wind speed $U(R)$) and turbulence intensity at the front, middle, and rear above the experiment platform are illustrated in Figure 7. The y -axis represents the cross-sectional height and the x -axis the normalized wind velocity or turbulence intensity. There is a little difference between the test wind profile and the

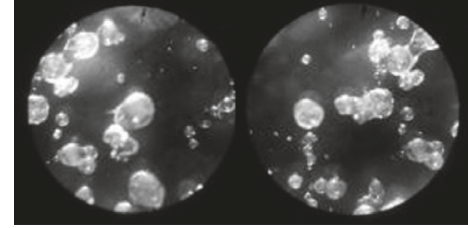


FIGURE 6: Shape of the artificial snow particles.

TABLE 2: Comparison of physical parameters of snow particles.

Kind of particles	Natural snow	Artificial snow
Diameter D_p (mm)	0.15~0.50	0.2~0.50
Particle density ρ_p (kg/m^3)	126~294	540~575
Bulk density ρ_b (kg/m^3)	90~210	386~411
Threshold friction velocity u_{*t} ($\text{m}\cdot\text{s}^{-1}$)	0.20	0.35
Angle of repose θ ($^\circ$)	30~50	45

TABLE 3: Experimental parameters of prototype and experiments.

Description	Prototype	Model
Geometrical scale ratio	1 : 1	1 : 30
Wind velocity at height of reference point	11.4 m/s	2.5 m/s
Wind duration	6 h	54 min

normalized wind profile; however, Anno [23] indicated that the shape of the wind profile did not play a major role in controlling the characteristic of the snowdrift by the wind tunnel test on snow fences, for the snowdrift pattern of the model with abrupt height changes, the small distortion of the wind profile is allowed. The box-type snow flux trapper draws on the design experience summarized by Kimura [31]; and snow flux along the height in the vertical plane was measured by additional experiments with only the snow flux trapper on the test ground. Snow flux along the vertical direction in the experiments is illustrated in Figure 8. The y -axis represents the height above the platform and the x -axis the volume of snow flowing past in one second per square meter. In these conditions, it was challenging to consider the similarity of snow flux. Considering that the experiments focused on snowdrift on the roof (0.2 m above the ground), it could not have had a large and unexpected impact on snow distribution on the roof even though a snow flux rate below 0.2 m is high. Thus, this similarity was ignored.

TABLE 4: Similarity parameters of prototype and scale model.

Dimensionless parameters	Prototype value	Model value (1/10 scale)
$(1 - (U_0/U))(U^2/Lg)$	0.163	0.166
UT/L	4104	4050
$u_{*t}^3/2g\gamma \geq 30$	—	146
$(u_{*t}^2/D_p g) \cdot (\rho/(\rho_p - \rho))$	0.050~0.068	0.054~0.065
ρ_p/ρ	97.4~227.4	417.6~444.8
$(u_{*t}^2/Lg) \cdot (\rho/(\rho_p - \rho))$	$0.321 \times 10^{-6} \sim 1.05 \times 10^{-5}$	$0.216 \times 10^{-5} \sim 1.67 \times 10^{-5}$

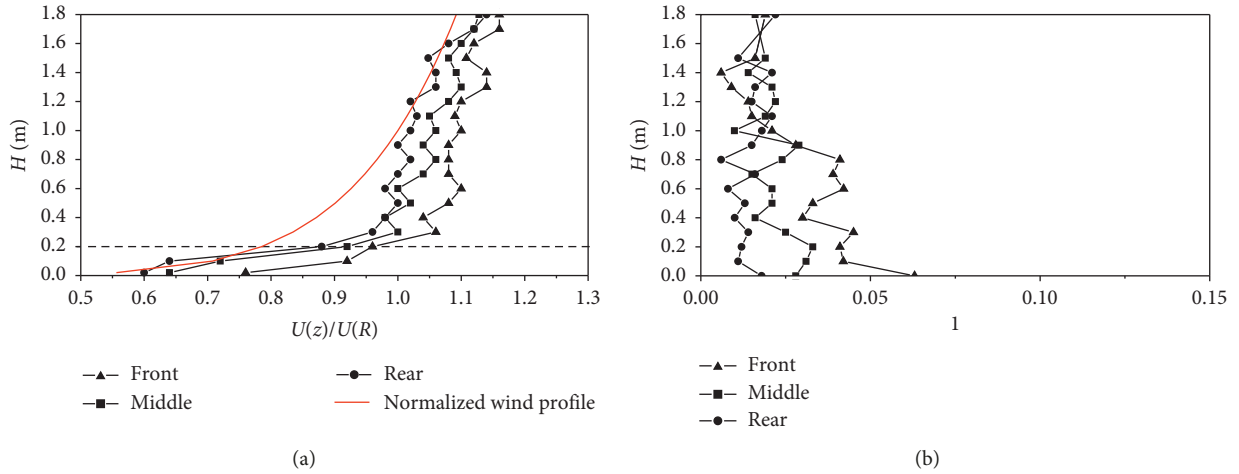


FIGURE 7: Variations in normalized mean (a) wind speed and (b) intensity of turbulence with height.

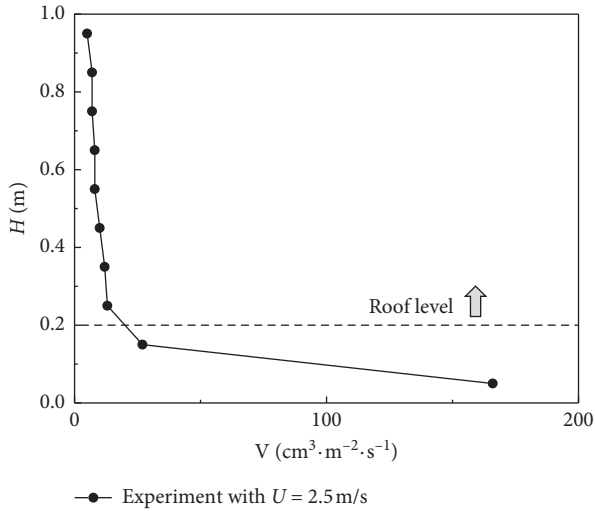


FIGURE 8: Snow flux along the vertical direction.

Snow depth was measured using a steel ruler by hand to accurately record the distribution of snow in the experiments. According to the horizontal projection area of the model, a measurement point was arranged every 5 cm for a total of 945 measurement points. During the test, the TC-4 automatic weather station was used to monitor external natural conditions, such as the natural wind environment, temperature, and humidity, in real time.

Wind direction is shown in Figure 9. Three experiments were designed to study the effect of wind direction when the

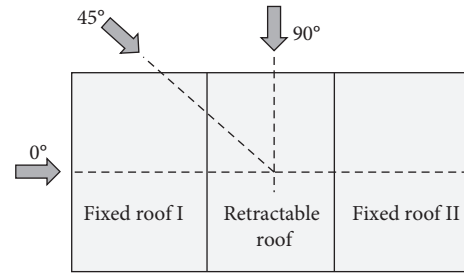


FIGURE 9: Sketch of the incidence angle of wind.

retractable roof was “closed.” The experimental conditions are listed in Table 5.

3.2. CFD Simulation of Snowdrift on Horizontally Retractable Roof. The steady method was used to simulate the drift of snow particles on the surface of the roof, and the transport equations of the air and snow phases were, respectively, established. It was assumed that the relationship between the two phases was one-way coupled—that is, snowdrifted under the action of wind (the air phase)—and the effects of the transport process and particle collision in the air were ignored.

The horizontally retractable roof model adopted for the CFD simulation is illustrated in Figure 10 and the mesh scheme is presented in Figure 11. The computation conditions are provided in Table 6 and the simulation conditions are outlined in Table 7. The initial snow depth is set as 0.3 m

TABLE 5: Details of experimental conditions.

Experiments	Wind direction	Wind speed	Temperature	Humidity	Testing time	State of retractable roof
(a)	0°	2.5 m/s	-6°C	61%	36 min	Closed
(b)	45°	2.5 m/s	-10°C	55%	36 min	Closed
(c)	90°	2.5 m/s	-9°C	55%	36 min	Closed

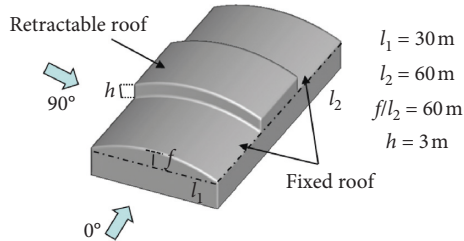


FIGURE 10: Horizontally retractable roof model.

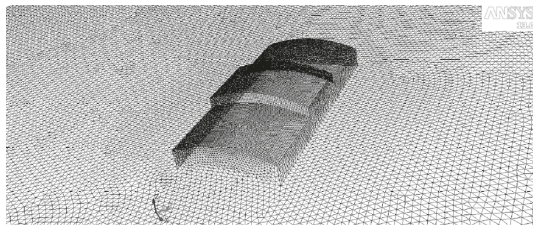


FIGURE 11: Mesh scheme of model.

corresponding to the snow load of 0.45 kN/m^2 (snow density equals 150 kg/m^3).

3.3. Comparison between Experimental Results and CFD Simulation. Figure 12 illustrates the results of the simulation of the distribution of snow. The snow load coefficient is the ratio of the depth of snow on the roof to the average snowfall S_d (for the experiments, S_d was determined by an additional experiment conducted for the same duration but without any obstacles in the test section, and at least 10 points with an interval greater than 10 cm in the experimental model area should be selected to calculate the average).

When the wind direction was 0° , there were three main snowdrifts on the roof: I was at the front of the fixed roof I, II was near the bottom of the retractable roof, and IV was in the middle of fixed roof II. The snowdrift obtained by the CFD method was in good agreement with that from the experiment in terms of both shape and value, except that the snow accumulated in area III was overestimated.

The above overestimation can be explained according to the wind field shown in Figure 13. Owing to the large length of the fixed roof on the windward side, the wind reattached at the front, and this caused wind speed in the nearby area to be low because of which a small amount of snow was deposited at the front of the roof. Near the junction with the movable roof, the wind had a small vortex scale and low wind speed because of which snow deposition occurred. On the leeward side, due to the reattachment of the wind to the central region and low wind speed, there occurred

remarkable snowdrift. The difference in snow accumulation at the leeward junction might have obtained because in the numerical simulation, the accumulation of snow was represented by the time integral according to the rate of snow deposition/erosion. However, although the wind speed was low enough to make the snow particles settle at the leeward junction, the source of snow particles in this area was mainly the reverse flow on the leeward roof, and fewer snow particles could enter this low-speed zone in snowfall. Thus, a large amount of snow was not accumulated.

When the wind direction was 45° , although there was considerable snowdrift in area I, snow mainly accumulated in area II and was distributed in a triangular shape. The reason for the difference at the junction on the leeward roof might have been identical to that in the case when wind direction was 0° .

When the wind direction was 90° , snow mainly accumulated on the leeward side of the arched roof, and its shape and magnitude as obtained through the numerical simulation and the experiment were in good agreement. This can be explained according to the wind field shown in Figure 14. The windward side of the roof is the acceleration zone and wind speed is relatively large; therefore, there is almost no snow accumulation. The wind field is separated at the rear end of the leeward side and a standing vortex is formed on the roof, so that large snow accumulation occurs. A difference occurred at the windward side of the roof, and the reason for it might be that wind speed in the experiment was reduced according to the similarity criterion so that snowdrift occurred in the reverse area at the front of the windward side of roof.

In particular, a significant change was evident in snow distribution on the roof. The area in which heavy accumulation occurred changed, and this indicates that wind direction had a significant effect on snow distribution.

Figures 15 and 16 illustrate snow distributions along the red line when the wind directions were 0° and 90° , respectively. The x -axis represents the relative position on the roof, the y -axis represents the normalized snow depth at any point, and S and S_d are the measured snow depth at any point and the average snowfall, respectively. It is evident that the snow distributions of the experiment and the CFD simulation on the windward side exhibited the same features in terms of distribution, but their extrema were slightly different, and the maximum snow depth in the CFD simulation was 10% smaller than that in the experiments. Moreover, by comparing snow depth on the leeward side, the two results were observed to be in agreement with each other, except when the snow depth was overestimated near the border between the retractable and fixed roofs. However, considering that this

TABLE 6: Computation conditions.

Conditions	Settings
Computational domain	850 m(x) * 250 m(y) * 60 m(z) (the building was located at 1/3 away from the entrance of airflow)
Number of elements	Approximately 4,800,000
Minimum mesh size	0.35 m
Inflow boundary	Wind velocity profile (see equation (7)), where v_0 and z_0 are 11.4 m/s and 6 m, respectively Snow fraction profile (see equation (8))
Outflow boundary	Zero gradient condition, the wind velocity gradient $\partial u/\partial n$ and snow fraction gradient $\partial f/\partial n$ are set to zero (outflow)
Upper face and side	Zero gradient condition for all variables, and the normal components of the wind velocity with respect to the boundaries are set to zero (symmetry)
Building and ground surface	No-slip boundary condition (wall), except that the wall roughness $z_0 = 5.0 \times 10^{-5}$ for the snow surface
Turbulence model	Realizable $k-\epsilon$ model
Multiphase model	Mixture model
Residual	10^{-7}

TABLE 7: Simulation conditions.

Experiments	Wind direction (°)	Wind speed (at 6 m height) (m/s)	State of retractable roof
(a)	0	11.4	Closed
(b)	45	11.4	Closed
(c)	90	11.4	Closed

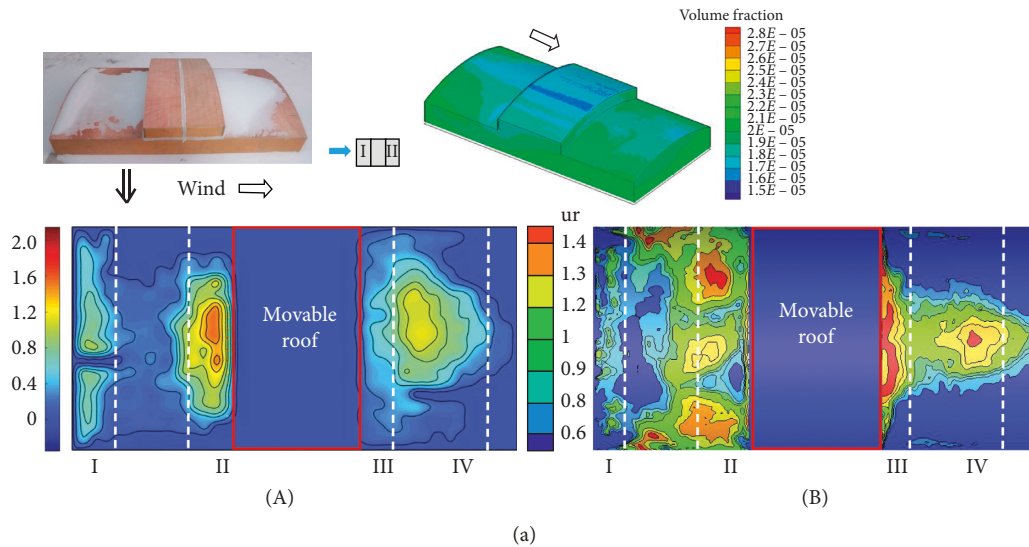


FIGURE 12: Continued.

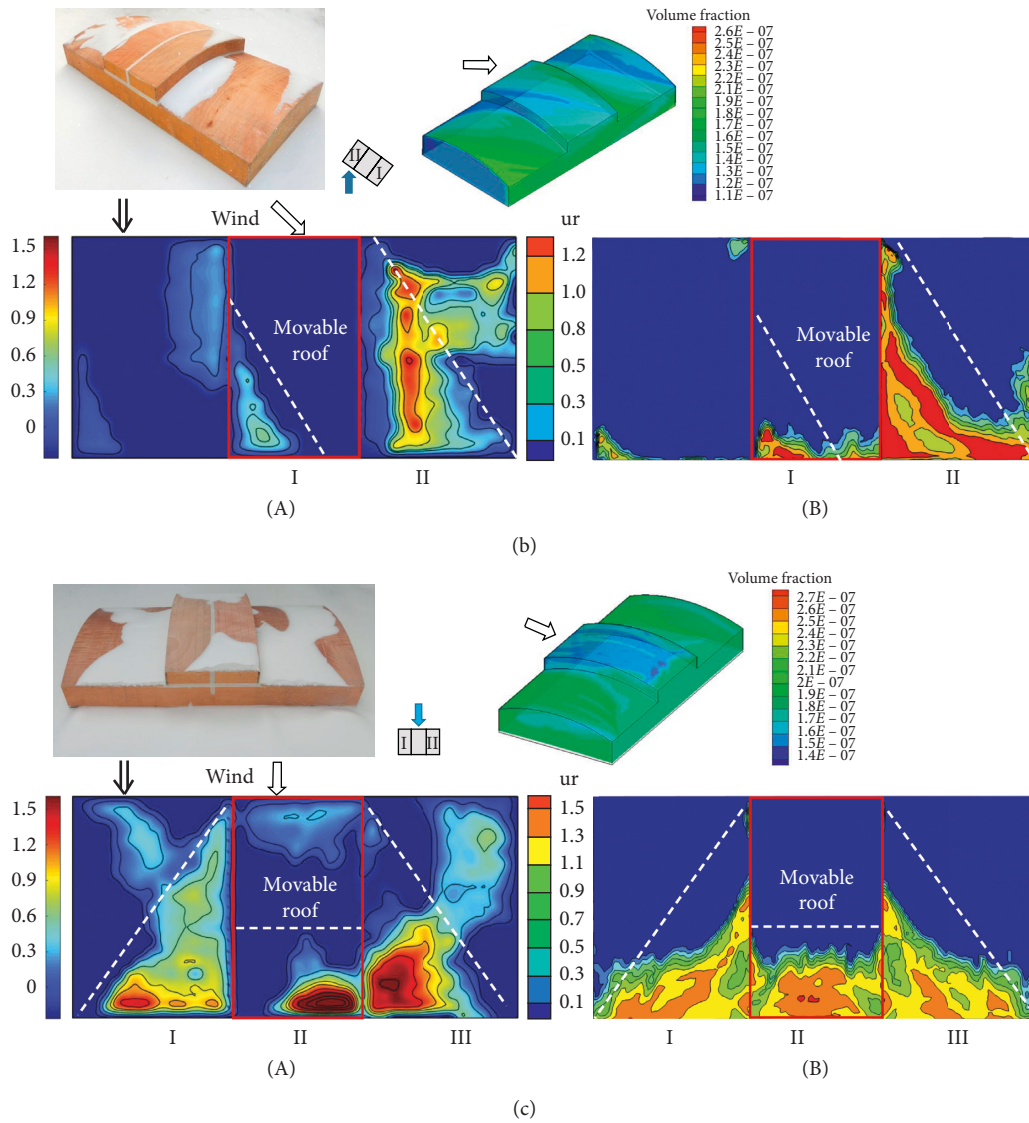


FIGURE 12: Comparison of results of experiments and simulations with different wind directions (A) Measurement (B) CFD simulation. (a) When wind direction is 0° . (b) When wind direction is 45° . (c) When wind direction is 90° .

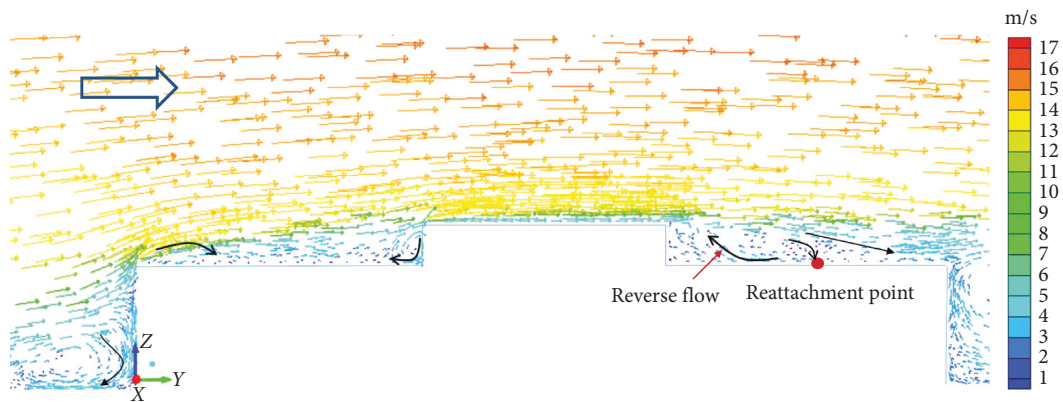


FIGURE 13: Wind speed vector at midsection when wind direction = 0° .

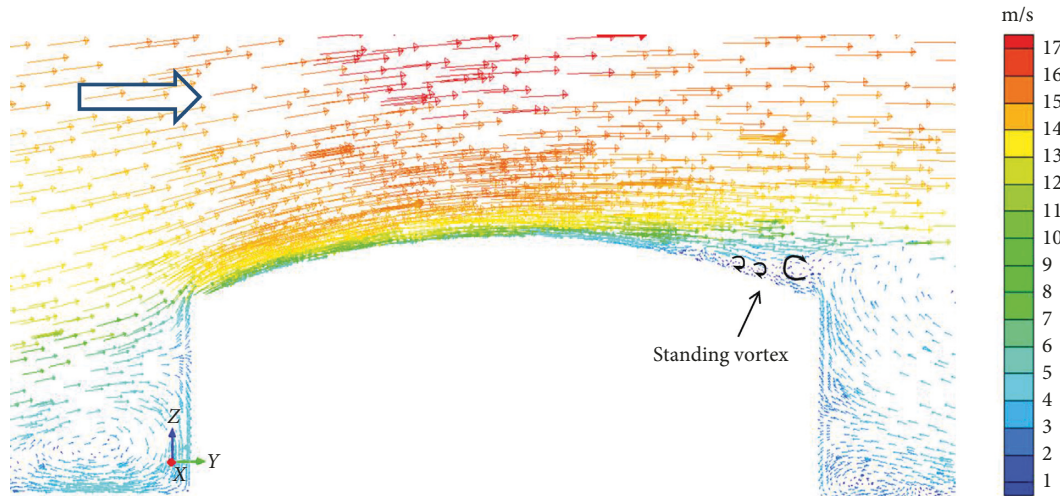


FIGURE 14: Wind speed vector at midsection when wind direction = 90°.

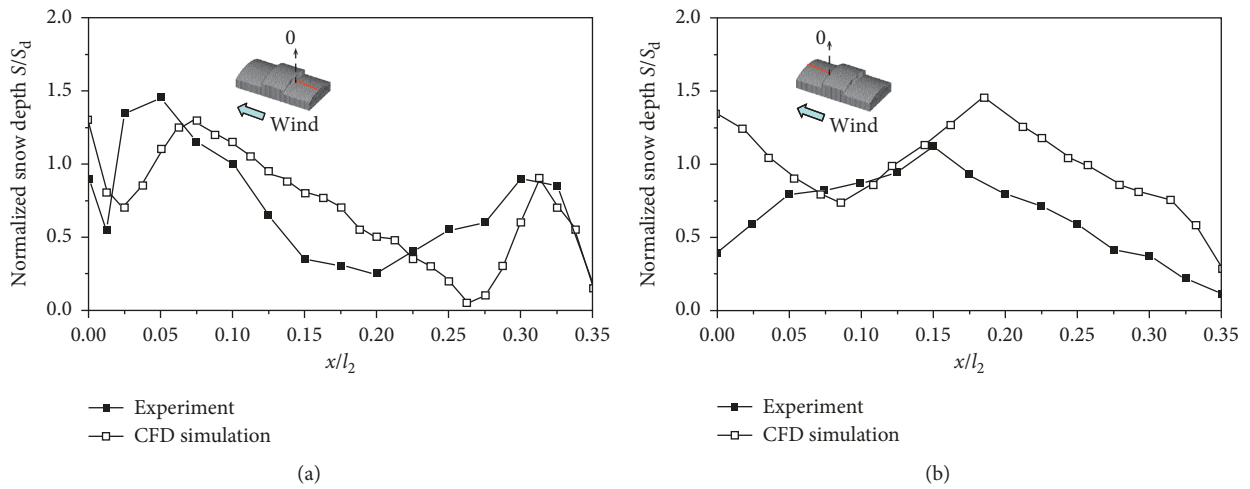


FIGURE 15: Comparison of results by means of experiments and CFD simulation along the central line when wind direction = 0°. (a) Windward side. (b) Leeward side.

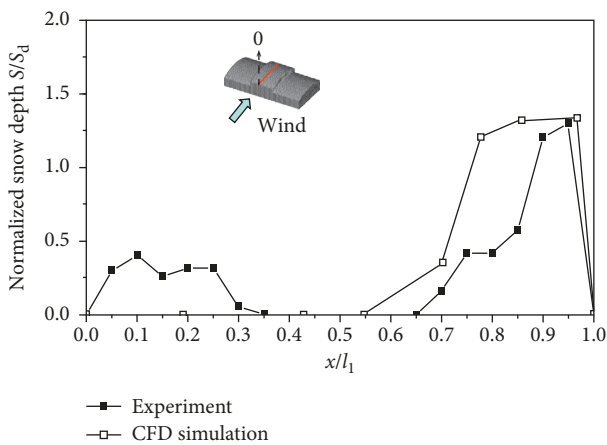


FIGURE 16: Comparison of results by means of experiments and CFD simulation along the central line when wind direction = 90°.

overestimation was conservative, the result obtained by the CFD simulation is acceptable.

Figure 16 shows that the results of the numerical simulation along the windward side show severe erosion and snow accumulation here had a coefficient of 0.6 in the test; on the leeward side, the numerical simulation shows that the extreme value of snow deposition was 5% greater than that in the experiment, and the positions of the extrema were all in the range $x/l_1 = 0.9 \sim 1.0$. The results on the leeward side agreed well with the experimental results.

The above analysis indicates that some differences persisted in the shape of the snow accumulated, but considering that the CFD method is reasonable at estimating the shape and magnitude of the accumulating snow in general, it is feasible and reliable for simulating snow distribution on retractable roofs.

4. Conclusions

In this paper, the accuracy of the CFD method in predicting snow distribution was analyzed according to a snowdrift simulation on a stepped roof model. Snow distribution on a typical retractable roof was investigated both by experiments and CFD simulations, and the conclusions drawn from the study are as follows:

- (i) According to the results of the snowdrift simulation on a stepped roof with different turbulence models, the result obtained by the realizable k - ϵ model exhibited better agreement with field observations in terms of 2D distribution than other models.
- (ii) A typical horizontally retractable roof model was selected to verify the accuracy of the CFD model in predicting the 3D distribution of snow loads on complex roofs. The results obtained from the experiments and numerical simulations were in good agreement for most snow accumulated, which further proves that numerical simulations can be used to estimate the distribution of snow load on the roofs of buildings.
- (iii) Under different wind directions, snow accumulation always occurred at the boundary between the movable roof and the fixed roof and the leeward side. The distribution of snow in the retractable roof can be determined by using directions of wind of 0° and 90° as unfavorable angles. We recommend installing snow removal equipment near the boundary of the movable roof.
- (iv) The numerical simulations and the experiments reflect the same law of snow deposition and erosion and the extrema of the obtained snow distribution were similar, but differences persisted in the specific area of deposition. This requires further study.

Nonuniform snow loads on retractable roofs are complex and significant to safety. Based on this study, several conclusions can be drawn using a simplified CFD method with dependent verification. However, this study has certain limitations, which will form the focus of future work:

- (i) When verifying the accuracy of the CFD method in predicting 3D distributions of snow loads on complex roofs, field observations of full-scale structures or large-scale models are required.
- (ii) Only the “closed” state of retractable roofs was considered. However, in the event of a sudden snowstorm, the retractable roof in its “open” state should also be taken into account.

Data Availability

The data used to support the findings of this study are included within the article. Previously reported data were used to support this study and are available at (DOI: 10.1016/j.jweia.2017.12.010). These prior studies (and datasets) are cited at relevant places within the text as references.

Conflicts of Interest

The authors declare that they have no conflicts of interest.

Acknowledgments

This work was conducted through the financial support of the National Natural Science Foundation of China (Project designation: 51878218 and 51378147).

References

- [1] X. Zhou, J. Hu, and M. Gu, “Wind tunnel test of snow loads on a stepped flat roof using different granular materials,” *Natural Hazards*, vol. 74, no. 3, pp. 1629–1648, 2014.
- [2] Y. Tominaga, “Computational fluid dynamics simulation of snowdrift around buildings: past achievements and future perspectives,” *Cold Regions Science and Technology*, vol. 150, pp. 2–14, 2018.
- [3] S. Alhajraf, “Computational fluid dynamic modeling of drifting particles at porous fences,” *Environmental Modelling & Software*, vol. 19, no. 2, pp. 163–170, 2004.
- [4] T. Okaze, H. Niiya, and K. Nishimura, “Development of a large-eddy simulation coupled with Lagrangian snow transport model,” *Journal of Wind Engineering and Industrial Aerodynamics*, vol. 183, pp. 35–43, 2018.
- [5] X. Zhou, L. Kang, M. Gu, L. Qiu, and J. Hu, “Numerical simulation and wind tunnel test for redistribution of snow on a flat roof,” *Journal of Wind Engineering and Industrial Aerodynamics*, vol. 153, pp. 92–105, 2016.
- [6] T. Uematsu, T. Nakata, K. Takeuchi, Y. Arisawa, and Y. Kaneda, “Three-dimensional numerical simulation of snowdrift,” *Cold Regions Science and Technology*, vol. 20, no. 1, pp. 65–73, 1991.
- [7] J. H. M. Beyers, P. A. Sundsbø, and T. M. Harms, “Numerical simulation of three-dimensional, transient snow drifting around a cube,” *Journal of Wind Engineering and Industrial Aerodynamics*, vol. 92, no. 9, pp. 725–747, 2004.
- [8] M. Beyers and B. Waechter, “Modeling transient snowdrift development around complex three-dimensional structures,” *Journal of Wind Engineering and Industrial*, vol. 96, no. 10–11, pp. 1603–1615, 2008.
- [9] Y. Tominaga, T. Okaze, and A. Mochida, “CFD modeling of snowdrift around a building: an overview of models and evaluation of a new approach,” *Building and Environment*, vol. 46, no. 4, pp. 899–910, 2011.
- [10] T. K. Thiis, J. Potac, and J. F. Ramberg, “3D numerical simulations and full scale measurements of snow depositions on a curved roof,” in *Proceedings of the 5th European & African Conference on Wind Engineering*, Florence, Italy, July 2009.
- [11] X. Sun, R. He, and Y. Wu, “Numerical simulation of snowdrift on a membrane roof and the mechanical performance under snow loads,” *Cold Regions Science and Technology*, vol. 150, pp. 15–24, 2018.
- [12] S. J. Wakes, “Use of CFD in the initial design of a snow fence,” in *Proceedings of the 7th International Congress on Environmental Modelling and Software*, San Diego, CA, USA, June 2014.
- [13] ANSYS, *ANSYS FLUENT Theory Guide*, ANSYS, Canonsburg, PA, USA, 2011.
- [14] Y. Hao, H. Liu, and Z. Chen, “Study on non-uniform snow load on single layer reticulated shell in Yujiapu,” *International*

- Journal of Space Structures*, vol. 22, no. 02, pp. 22–27, 2016, in Chinese.
- [15] M. Naaim, F. Naaim-Bouvet, and H. Martinez, “Numerical simulation of drifting snow: erosion and deposition models,” *Annals of Glaciology*, vol. 26, pp. 191–196, 1998.
- [16] AIJ, *AIJ Recommendations for Loads on Buildings*, AIJ, Tokyo, Japan, 2004.
- [17] J. W. Pomeroy and D. M. Gray, “Saltation of snow,” *Water Resources Research*, vol. 26, no. 7, pp. 1583–1594, 1990.
- [18] J. W. Pomeroy and D. H. Male, “Steady-state suspension of snow,” *Journal of Hydrology*, vol. 1–4, no. 136, pp. 275–301, 1992.
- [19] Y. Tominaga and A. Mochida, “CFD prediction of flowfield and snowdrift around a building complex in a snowy region,” *Journal of Wind Engineering and Industrial Aerodynamics*, vol. 81, no. 1–3, pp. 273–282, 1999.
- [20] T. Okaze, Y. Takano, A. Mochida, and Y. Tominaga, “Development of a new k- ϵ model to reproduce the aerodynamic effects of snow particles on a flow field,” *Journal of Wind Engineering and Industrial Aerodynamics*, vol. 144, pp. 118–124, 2015.
- [21] M. Tsuchiya, T. Tomabechi, T. Hongo, and H. Ueda, “Wind effects on snowdrift on stepped flat roofs,” *Journal of Wind Engineering and Industrial Aerodynamics*, vol. 90, no. 12–15, pp. 1881–1892, 2002.
- [22] M. Liu, Q. Zhang, F. Fan, and S. Shen, “Experiments on natural snow distribution around simplified building models based on open air snow-wind combined experimental facility,” *Journal of Wind Engineering and Industrial Aerodynamics*, vol. 173, pp. 1–13, 2018.
- [23] Y. Anno, “Requirements for modeling of a snowdrift,” *Cold Regions Science and Technology*, vol. 8, no. 3, pp. 241–252, 1984.
- [24] J. D. Iversen, “Comparison of wind-tunnel model and full-scale snow fence drifts,” *Journal of Wind Engineering and Industrial Aerodynamics*, vol. 8, no. 3, pp. 231–249, 1981.
- [25] R. J. Kind, “A critical examination of the requirements for model simulation of wind-induced erosion/deposition phenomena such as snow drifting,” *Atmospheric Environment*, vol. 10, no. 3, pp. 219–227, 1976.
- [26] R. J. Kind, “Snowdrifting: a review of modelling methods,” *Cold Regions Science and Technology*, vol. 12, no. 3, pp. 217–228, 1986.
- [27] R. J. Kind and S. B. Murray, “Saltation flow measurements relating to modeling of snow drifting,” *Journal of Wind Engineering and Industrial Aerodynamics*, vol. 10, no. 1, pp. 89–102, 1982.
- [28] F. Naaim-Bouvet, “Comparison of requirements for modeling snowdrift in the case of outdoor and wind tunnel experiments,” *Surveys in Geophysics*, vol. 16, no. 5-6, pp. 711–727, 1995.
- [29] R. D. Tabler, “Self-similarity of wind profiles in blowing snow allows outdoor modeling,” *Journal of Glaciology*, vol. 26, no. 94, pp. 421–434, 1980.
- [30] H. Mo, F. Fan, and H. Hong, “Evaluation of input wind speed used in wind tunnel test and numerical simulation to estimate drifting snow profile,” *Journal of Building Structures*, vol. 36, no. 7, pp. 75–80, 2015, in Chinese.
- [31] T. Kimura, “Measurements of drifting snow particles,” *Journal of Geography (Chigaku Zasshi)*, vol. 100, no. 2, pp. 250–263, 1991.

